Derivation and numerical resolution of 2D Shallow Water equations for multi-regime flows of Herschel-Bulkley fluids

David Michuri, Jerome Monnier, Mathieu Sellier

Derivation and numerical resolution of 2D Shallow Water equations for multi-regime flows of Herschel-Bulkley fluids

David Kibe Muchiri[a,b], Jerome Monnier[b] and Mathieu Sellier[a]

[a]Department of Mechanical Engineering, University of Canterbury, Christchurch 8140, New Zealand.
[b]INSA & Institut de Mathématiques de Toulouse (IMT), 31400 Toulouse, France.
Correspondence author: jerome.monnier@insa-toulouse.fr

Abstract

This paper presents mathematical modeling and simulation of thin free surface flows of viscoplastic fluids with a Herschel-Bulkley rheology over complex topographies. Using asymptotic expansion method, depth-averaged models (lubrication and Shallow Water type models) are derived for three-dimensional multi-regime flows on non-flat inclined topographies with varying basal conditions. Starting from the reference solutions (zeroth-order ones), flow models are calculated as perturbations of these reference solutions. Two flow regimes corresponding to different balances between shear and pressure forces are presented. The classical flow models in the literature (corresponding to the first regime) are recovered by considering their respective cases on a flat-inclined surface. In the second regime case, a pressure term is non-negligible. Mathematically it leads to a corrective term to the classical regime equations. Using dimensionless parameters, the two regimes flow solutions are compared; the differences appear in the vicinity of sharp changes of slopes. Comparisons of numerical results with dam-break experiments in different geometries are presented for validation.

Key words: Shallow Water equations, viscoplastic, Herschel-Bulkley rheology, free-surface flows, multi-regime flows, depth-integrated models.

1 Introduction

Mathematical modeling and simulation of gravity driven thin surface flows (e.g. lava flows), has a number of important geophysical and engineering applications. One key application is the ability to predict the fluid rheology for risk assessments and hazard management plans. Reliable forecasting, however, prompts for accurate modeling of the flow dynamics. This paper aims at deriving a mathematical model that is adequate to simulate Herschel-Bulkley fluids, in particular for real-like lava flows.

In fluid mechanics, lava is categorized as an example of a viscoplastic material because of its yield stress threshold, beyond which it flows like a fluid and below which it behaves like a rigid solid. Other examples common in nature and with such complex behavior are mud flows and snow avalanches. Examples of viscoplastic materials for industrial applications include, but are not limited to, food pastes, cosmetic creams,

coating films and other concentrated suspensions [1, 2, 8]. There is a vast literature on viscoplastic flows, see for instance [1, 2, 6, 8, 12]. A number of mathematical models describing this complex rheology of viscoplastic flows have been suggested and studied. The most common are the Bingham model and the Herschel-Bulkley model [1, 5, 30]. Generally, the Herschel-Bulkley model, is widely used because of its ability to describe many complex fluid behaviors in a non-linear and history independent manner. For instance, the Herschel-Bulkley model has been applied for viscoplastic flows on an inclined surface in [6, 30] and its comparison with dam-break experiments presented in [3, 15, 16].

Apart from the complex rheology, modeling of geophysical viscoplastic flows still remains an active topic of research because of the complex topography that evolve rapidly, the extreme temperatures involved especially for lava flows and the uncertainty of data required to verify the model. Moreover, these flows have an additional complexity arising from the evolution of the free surface with time. Solving the full set of Navier-Stokes equations governing these flows thus becomes computationally expensive and difficult. However, some free surface flows are characterized by a small thickness compared to the characteristic length which makes it possible to reduce the three-dimensional flow configuration to a lower dimension by depth-averaging approaches [14, 35, 36]. Depth-averaged models, also known as depth-integrated models, are less expensive to solve compared to the full Navier-Stokes equations.

The depth integrated models presented in this paper comprise of the Lubrication model and the Shallow Water equations model. Lubrication model result from a hypothesis that the fluid considered is relatively shallow and inertial effects are small [5, 14, 28]. It has been derived and studied for long in many thin free surface flows. One key advantage of lubrication approximation is that it results to a one-equation model governing the evolution of the fluid depth which is much less expensive to solve. However, this model is over-simplified and may fail to capture all important flow details [5, 19, 27, 30], for instance, the inertial terms are neglected at order zero. For shallow flows, this model is also not consistent with wet-dry front dynamics as the depth approaches zero, see [11, 13, 19, 25] and references therein.

On the other hand, the Shallow Water equations model is obtained by averaging the local mass and momentum conservation equations over the fluid depth, resulting in a two-equations model. It is more consistent than lubrication model, for instance the inertial terms are not inconsequential, see e.g. [11, 19, 28] and references therein. The Shallow Water equations were first introduced by Barré de Saint-Venant for Newtonian hydraulic flows in 1887 [18]. Since then, derivation and use of the Shallow Water equations have been extended to non-Newtonian flows using asymptotic expansion methods. For instance, Shallow Water models for power-law fluids and Bingham fluids based on asymptotic expansion of the Cauchy Momentum equations have been derived in [19, 28], derivation of the Saint-Venant equations for free surface flows of viscoplastic fluids on a flat inclined plane has been documented in [9, 10, 12]. Both Lubrication type and Shallow Water type models have widely been used to study thin free surface flows with different flow configurations. [12] derived the Saint-Venant equations model for viscoplastic flows with Herschel-Bulkley rheology on a flat inclined plane, [11] derived asymptotic thin layer flow models (one equation and two equation type) for power-law fluids with varying basal boundary conditions (corresponding to multi-regimes), [23] derived a two-dimensional viscous Shallow Water model with irregular topography, bottom friction and capillary effects, [33] derived a three equation model corresponding to mass, momentum and energy equation, for thin viscous film on an inclined plane. The present article builds on the derivation of these models in particular the Shallow Water equations partly presented in [12] and [11] and extended to a 2-D model on a non-flat inclined configuration with varying conditions at bottom, therefore potentially presenting different flow regimes which are naturally defined in function of dimensionless parameters.

The outline of the paper is organized as follows. In Section 2, the flow configuration and the governing equations are defined. By scaling and introducing dimensionless variables, the primitive equations are non-dimensionalized. The orders of magnitude of dimensionless parameters and the weight coefficients from field measurements of lava flows are also tabulated and analyzed following [11], in order to define the appropriate flow regimes for consideration. In Section 3, zeroth-order solutions equivalent to steady uniform state solutions are calculated. These flow solutions are important as they serve as reference solutions when calculating solutions of other flow models. In Section 4, the one-equation model of lubrication type is derived. Two shear regimes are defined: Regime A (standard regime) corresponding to the zeroth-order solutions and regime B (enriched regime) with an additional corrective term. By depth-averaging, the Shallow-Water equations are derived in Section 5, using asymptotic analysis following [11, 12]. The equations are converted to physical form and considering particular cases in the literature, classical models are recovered. Numerical results of the Shallow Water equations are presented in Section 6. Model predictions are compared with experimental results of dam-break flows [15,16,29]. Steady flow solutions with a bump at the center are then plotted for analysis - to distinguish the two shear regimes. Final conclusions are drawn in Section 7.

2 Model formulation

Consider a 2D flow configuration of a thin layer of a viscoplastic lava-like fluid on an inclined topography as shown in Fig. 1, with x being the axis of the slope at an angle θ and z, the axis normal to the slope. The flow is driven by gravity $\underline{g} = (g\sin\theta, -g\cos\theta)$ and described by its velocity $\underline{u} = (u, w)$ and pressure field denoted by p. The fluid evolves within a time-dependent domain $\Omega(t) = \big\{(x,z)\in\mathbb{R}^2 : b(x) \le z \le H(t,x)\big\}$, where $H(t,x,z)$ is the fluid elevation, $b(x,z)$ the basal topography elevation and $h(t,x,z) = H(t,x,z) - b(x,z)$ the fluid depth.

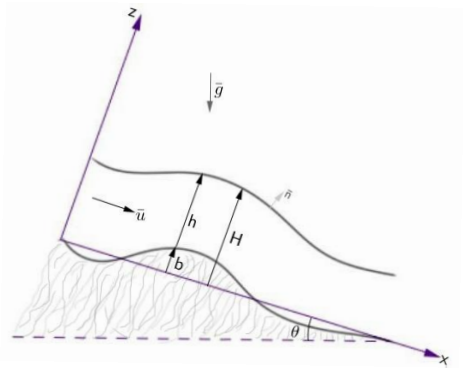

Figure 1: Flow configuration with non-flat topography

The flow dynamics are described by the incompressibe Navier-Stokes equations (conservation of mass and momentum, respectively) together with the Herschel-Bulkley constitutive law:

$$\begin{aligned} &\partial_x u + \partial_z w = 0, \\ &\rho(\partial_t u + u\partial_x u + w\partial_z u) = -\partial_x p + \rho g\sin\theta + \partial_x\sigma_{xx} + \partial_z\sigma_{xz}, \\ &\rho(\partial_t w + u\partial_x w + w\partial_z w) = -\partial_z p - \rho g\cos\theta + \partial_x\sigma_{zx} + \partial_z\sigma_{zz}, \end{aligned} \tag{2.1}$$

with $\underline{\underline{\sigma}} = \underline{\underline{\tau}} + p\underline{\underline{I}}$, where τ is the total stress tensor, $\underline{\underline{\sigma}} = \begin{pmatrix} \sigma_{xx} & \sigma_{xz} \\ \sigma_{zx} & \sigma_{zz} \end{pmatrix}$ the deviatoric stress tensor and $\underline{\underline{I}}$

the identity tensor.

The Herschel-Bulkley rheology law reads

$$\begin{cases} \sigma_{ij} = \left(K(T)\dot{\gamma}^{n-1} + \frac{\tau_c}{\dot{\gamma}}\right)\dot{\gamma}_{ij} & \text{for} \quad \tau > \tau_c, \\ \dot{\gamma}_{ij} = 0 & \text{for} \quad \tau \leq \tau_c, \end{cases} \tag{2.2}$$

where $\dot{\gamma}_{ij} = \partial_j u_i + \partial_i u_j$ are elements of the the strain rate tensor, $\dot{\gamma} = \sqrt{\frac{1}{2}\sum_{ij}\dot{\gamma}_{ij}\dot{\gamma}_{ij}}$ the Frobenius norm of the deformation tensor, τ the stress norm, $n > 0$ the power-law index, T the fluid temperature, $K(T) > 0$ the consistency index and τ_c the yield stress.

Other fluid models can be recovered using this law (2.2) depending on n and τ_c. For instance, when $n = 1$, the Herschel-Bulkley model reduces to Bingham model where the consistency index K becomes the plastic viscosity η. When $n < 1$ the model reduces to shear thinning fluid (pseudo-plastic) in which the apparent viscosity increases the shear rate. For $n > 1$, the fluid is shear thickening (dilatant). When $n \neq 1$ and $\tau_c = 0$, a power-law fluid model is obtained. When $n = 1$ and $\tau_c = 0$, the Herschel-Bulkley model reduces to Newtonian fluid model and $K(T)$ becomes the viscosity of the fluid.

The above governing equations are subject to the following boundary conditions:

- Boundary conditions at the bottom surface, $z = b$. This comprise of the friction condition otherwise known as the power-law type condition or Weertman-type friction law (see e.g. [11]), given as

$$\begin{cases} \underline{u} \cdot \underline{t}_b = -C|\underline{\underline{\sigma}} \cdot \underline{n}_b \cdot \underline{t}_b|^{\frac{1-n}{n}} \underline{\underline{\sigma}} \cdot \underline{n}_b \cdot \underline{t}_b, \\ \underline{u} \cdot \underline{t}_b = 0, \end{cases} \tag{2.3}$$

  where C is the basal slip coefficient, $\underline{n}_b$ the outward normal to the bottom and $\underline{t}_b$ the tangent to the bottom. The negative sign allows C to be positive since $\underline{n}_b$ is pointing outward. When $C = 0$, the no slip condition is recovered: $u = 0$ and $w = 0$.

- Boundary conditions at the free surface $z = H$ comprised of

  - ◇ No stress condition: $\underline{\underline{\tau}} \cdot \underline{n} = 0$ where unit normal $\underline{n} = \frac{1}{\sqrt{1+(\partial_x H)^2}}\begin{pmatrix}\partial_x H \\ -1\end{pmatrix}$. With some computations, this gives rise to two expressions: $\sigma_{xz} = \frac{\partial_x H}{1-(\partial_x H)^2}(\sigma_{xx} - \sigma_{zz})$ and $p = \frac{1}{1-\partial_x H}(\sigma_{zz} - (\partial_x H)^2\sigma_{xx})$.
  - ◇ Kinematic condition: $\partial_t h + u\partial_x H = w$.

Since the flow is incompressible, the mass conservation in Eq (2.1) results in the following equality: $\partial_x u = -\partial_z w \Leftrightarrow \sigma_{xx} = -\sigma_{zz}$.

2.1 Scaling and non-dimensionalization

For non-dimensionalization of the primitive equations, L is set to be the characteristic length in the direction of the flow, $\mathcal{H}$ the characteristic depth, U the scale of u and W the scale of w. By scaling and

introducing dimensionless variables denoted by $'$ yields: $x = Lx'$, $z = \mathcal{H}z'$, $t = \frac{L}{U}t'$, $b = \mathcal{H}b'$, $h = \mathcal{H}h'$, $H = \mathcal{H}H'$, $u = Uu'$ and $w = Ww'$. Assuming thin flow, such that the characteristic fluid depth $\mathcal{H}$ is much smaller than the corresponding characteristic length L, a geometric scaling parameter can be defined as $\epsilon = \frac{\mathcal{H}}{L} << 1$. From the mass conservation equation, it can be deduced: $W = \frac{\mathcal{H}}{L}U$. For the pressure p, a hydrostatic pressure scale can be chosen as: $p = \rho g \mathcal{H} cos\theta p'$. Some standard scales are adopted for deviatoric stresses: $\sigma_{xx} = \frac{KU^n}{\mathcal{H}^{n-1}L}\sigma'_{xx}$, $\sigma_{zz} = \frac{KU^n}{\mathcal{H}^{n-1}L}\sigma'_{zz}$and $\sigma_{xz} = K\left(\frac{U}{\mathcal{H}}\right)^n \sigma'_{xz}$. The strain rate is scaled naturally as: $\dot{\gamma} = \frac{U}{\mathcal{H}}\dot{\gamma}'$. Injecting these dimensionless variables into the primitive equations, some standard dimensionless numbers can be defined: the Reynolds number: $Re = \frac{\rho U^{2-n}\mathcal{H}^n}{K}$, the Froude number: $Fr = \frac{U}{\sqrt{g\mathcal{H}\cos\theta}}$ and the Bingham number: $Bi = \frac{\tau_c}{K}\left(\frac{\mathcal{H}}{U}\right)^n$.

Following the work of [11, 19, 28], some dimensionless parameters that occur naturally can be deduced:

$$\beta = \epsilon Re, \quad \alpha = \epsilon\gamma, \quad \delta = \frac{\epsilon}{\gamma}, \quad \text{and} \quad \lambda = \frac{1}{\gamma}\tan\theta,$$

where β, α and δ are weight coefficients corresponding to the inertial term, viscous term and the pressure term respectively. λ is the normalized gravity source term where $\gamma = \frac{Fr^2}{Re}$. For mathematical convenience we set $m = \frac{1}{n}$, where n is the power-law index. Dropping the $'$ notation, the following equations are obtained in non-dimensional form:

- Conservation of mass and momentum, respectively:

$$\begin{aligned} &\partial_x u + \partial_z w = 0. \\ &\beta(\partial_t u + u\partial_x u + w\partial_z u) = -\delta\partial_x p + \lambda + \alpha\delta\partial_x\sigma_{xx} + \partial_z\sigma_{xz}, \\ &\epsilon^2\beta(\partial_t w + u\partial_x w + w\partial_z w) = -\delta(\partial_z p + 1) + \alpha\delta(\partial_x\sigma_{xz} + \partial_z\sigma_{zz}). \end{aligned} \tag{2.4}$$

- The scaled friction condition at $z = b$ writes (see e.g [11])

$$\begin{cases} u &= C\frac{\left|\sigma_{xz}\left(1-\alpha\delta\partial_x b\right)^2 - 2\alpha\delta\sigma_{xx}\partial_x b\right|^{m-1}}{\left(1+\alpha\delta\partial_x b^2\right)^{m+\frac{1}{2}}}\left(\sigma_{xz}\left(1-\alpha\delta\partial_x b\right)^2 - 2\alpha\delta\sigma_{xx}\partial_x b\right), \\ w &= u\partial_x b. \end{cases} \tag{2.5}$$

- Boundary conditions at $z = H$: the no stress condition resulting to two expressions:

$$\sigma_{xz} = \frac{\alpha\delta\partial_x H}{1-\alpha\delta(\partial_x H)}(\sigma_{xx} - \sigma_{zz}), \quad p = \frac{\alpha}{(1-\alpha\delta(\partial_x H)^2)}(\sigma_{zz} - \alpha\delta(\partial_x H)^2\sigma_{xx}). \tag{2.6}$$

  and the Kinematic condition: $\partial_t h + u\partial_x H - w = 0$.

- Rheological law:

$$\begin{cases} \sigma_{xx} = -\sigma_{zz} = 2\left(\frac{Bi}{\dot{\gamma}} + \dot{\gamma}^{n-1}\right)\partial_x u, & \\ \sigma_{xz} = \left(\frac{Bi}{\dot{\gamma}} + \dot{\gamma}^{n-1}\right)(\partial_z u + \alpha\delta\partial_x w) & \text{for} \quad \tau > Bi, \\ \dot{\gamma}_{ij} = 0 & \text{for} \quad \tau \leq Bi, \end{cases} \tag{2.7}$$

  where $\dot{\gamma} = \sqrt{\left(\partial_z u + \alpha\delta\partial_x w\right)^2 + 4\alpha\delta\left(\partial_x u\right)^2}$, $\dot{\gamma}_{ij} = \begin{pmatrix} 2\epsilon\partial_x u & \partial_z u + \alpha\delta\partial_x w \\ \partial_z u + \alpha\delta\partial_x w & -2\epsilon\partial_x u \end{pmatrix}$ and $\tau = \sqrt{\sigma_{xz}^2 + \alpha\delta\sigma_{xx}^2}$.

2.2 Orders of magnitude of dimensionless parameters

Field measurements of lava flows sourced from [8, 20, 21] are presented in Table 1 for analysis. The corresponding orders of magnitude of dimensionless parameters and weight coefficients are calculated as shown in Table 2. The density of lava and inclination angle used for this calculations is $\rho = 2700kg/m^3$ and $\theta = 10^o$ respectively. From the order of magnitude in Table 2, the following deductions can be

	Composition	Temperature, θ (^0C)	Viscosity, K (Pas)	Velocity, u (m/s)
Less viscous lava	Komatiite	$1400 - 1600$	10^0	10^1
Viscous lava (Intermediate)	Basalt	1200	10^2	10^{-1}
More viscous lava	Dacite/Rhyolite	900	10^7	10^{-2}

Table 1: Measurements of 3 types of lava flows, [8, 20, 21].

	ϵ	Re	Fr	β	α	δ	λ	$\frac{1}{\beta}$	$\frac{\delta}{\beta}$	$\frac{\alpha\delta}{\beta}$
Less viscous lava	10^{-5}	10^3	10^1	10^{-2}	10^{-7}	10^{-4}	10^1	10^1	10^3	10^{-9}
Viscous lava (Intermediate)	10^{-3}	10^0	10^{-2}	10^{-3}	10^{-7}	10^1	10^3	10^2	10^5	10^{-3}
More viscous lava	10^{-2}	10^{-5}	10^{-3}	10^{-7}	10^{-3}	10^{-1}	10^0	10^7	10^6	10^3

Table 2: Orders of magnitude of dimensionless parameters and weight coefficients.

made: the aspect ratio is small in the three regimes, which validates the long wave assumption: $\epsilon << 1$. Numerical investigations have shown that, the shallow layer assumption is numerically valid up-to $\epsilon \approx 0.3$, see e.g., [20, 24]. The dimensionless parameter α is negligibly small in the three regimes. β is very small in more viscous lava compared to other flow regimes, hence important when distinguishing the three regimes. On the other hand, δ is either small or of at most order 1. This implies that real flows are multi-regimes in (β, δ). The gravity term λ is of at most order 3 and can be much higher in steep slopes. Reynolds number Re and Froude number Fr for less viscous lava (and intermediate lava) are much higher than those of more viscous lava, which rules out consideration of the more viscous lava in this paper. Generally, Komatiite and Basaltic lava which are less viscous, are the most common lava flows on earth [20]. From this analysis two regimes depending on β, α and δ can be defined:

- Regime A: with β small, α small and δ small (Less viscous lava).
- Regime B: with β small, α small while $\delta = O(1)$) (Intermediate viscous lava).

Considering these two regimes, the weight coefficient $\frac{\alpha\delta}{\beta}$ as seen in Table 3, is much smaller than other terms, it can thus be neglected - this will be recalled in the following sections. The asymptotic models corresponding to these two regimes will be derived in the next sections.

3 Zeroth-order solutions

Zeroth-order approximation of the primitive equations results to steady uniform solutions (here in dimensionless form). These solutions are important since they serve as the reference solutions for other flow

regimes (see e.g. [11, 12, 28]). Zeroth-order solutions are achieved by assuming a uniform flow ($h = \text{const}$) in x direction on a flat inclined bed ($b \equiv 0$), see Fig. 2 and by setting $\beta = \delta = \alpha = 0$. Thus, the governing equations (2.4-2.7) simplifies to:

- Momentum equation:
$$\begin{cases} \partial_z \sigma_{xz} = -\lambda, \\ \partial_z p = -1. \end{cases} \tag{3.1}$$

- Rheological law:
$$\begin{cases} \sigma_{xz} = Bi + (\partial_z u)^n & \text{if} \quad \sigma_{xz} > Bi, \\ \partial_z u = 0 & \text{if} \quad \sigma_{xz} \leq Bi, \end{cases} \tag{3.2}$$
where at order zero; $\tau = \sigma_{xz}$ and $\dot{\gamma} = \partial_z u$.

- Friction condition at $z = 0$: $u = C|\sigma_{xz}|^{m-1}\sigma_{xz}$, $w = 0$, from which a non-slip condition is recovered when the slip coefficient $C = 0$ and pure slip when $C \to \infty$.

- Boundary conditions at the free surface $z = h$: $\sigma_{xz} = 0$, and $p = 0$.

(a) (b)

Figure 2: Sketch of steady uniform flow (a) and lubrication regime (b) showing plug and sheared zones in Herschel-Bulkley flows

Solving Eq. (3.1) a hydrostatic pressure and shear stress which are linear in z are obtained:

$$p = h - z, \quad \sigma_{xz} = \lambda\,(h - z)\,. \tag{3.3}$$

Consequently, the friction condition at $z = 0$ reduces to $u = C\,(\lambda h)^m$ and $w = 0$. Near the free surface as $z \to h$, the shear stress component $\sigma_{xz} \to 0$. This implies the existence of a plug like flow near the free surface of thickness h_p (see Fig. 2) such that

$$h_p = \frac{Bi}{\lambda}. \tag{3.4}$$

Next, solving for stream-wise velocity using Eqs. (3.2), (3.3) and (3.4) yields

$$u(z) = \begin{cases} \frac{1}{m+1}\lambda^m h_c^{m+1}\left[1 - \left(1 - \frac{z-b}{h_c}\right)^{m+1}\right] + C(\lambda h)^m, & \text{for} \quad z < h_c \\ \frac{1}{m+1}\lambda^m h_c^{m+1} + C(\lambda h)^m, & \text{for} \quad z \geq h_c \end{cases} \tag{3.5}$$

where $h_c = \max(0, h - h_p)$ represents the thickness of the sheared zone below the plug. The flow rate can also be obtained by $q = h\bar{u} = \int_b^H u dz$ where $\bar{u}$ is the mean velocity:

$$q = \lambda^m h_c^{m+1} \left[\frac{1}{m+1} h_p + \frac{1}{m+2} h_c \right] + C\lambda^m h^{m+1}. \tag{3.6}$$

In a Newtonian case where $Bi = 0$, $m = 1$ and taking $C = 0$, the plug is absent, thus $h_c = h$. This results in a Poiseuille-like velocity profile: $u(z) = \frac{1}{2}\lambda h^2 \left[1 - \left(1 - \frac{z}{h}\right)^2\right]$, and the average velocity $\bar{u}$ in terms of thickness h becomes $\bar{u} = \frac{1}{3}\lambda h^2$.
Steady uniform solution is important as it gives an idea of how the flow behaves and serves as a reference for other flow regimes. Asymptotic fields of other flow regimes considered in the following sections, are calculated as perturbations of this reference flow.

4 Lubrication type model (one-equation model)

In the lubrication theory, it is assumed that one dimension is significantly smaller than the others, here the geometrical ratio $\epsilon = \frac{H}{L} << 1$, and that the inertial terms are inconsequential. To obtain the lubrication model otherwise known as the one-equation model, the 0^{th} order terms in ϵ are considered: $\beta = \alpha = O(\epsilon)$. As a result, the model (2.4-2.7) is reduced to the following system of equations:

- Conservation of mass: $\partial_x u + \partial_z w = 0$, and the conservation of momentum:

$$\partial_z \sigma_{xz} = \delta \partial_x p - \lambda, \tag{4.1}$$

$$\partial_z p = -1. \tag{4.2}$$

- Herschel-Bulkley rheology law:

$$\begin{cases} \sigma_{xx} = -\sigma_{zz} = 2\left(\frac{Bi}{\partial_z u} + (\partial_z u)^{n-1}\right)\partial_x u, & \\ \sigma_{xz} = Bi + (\partial_z u)^n & \text{for} \quad \sigma_{xz} > Bi, \\ \partial_z u = 0 & \text{for} \quad \sigma_{xz} \leq Bi, \end{cases} \tag{4.3}$$

- Friction boundary condition at the bottom surface $z = b$: $u = C|\sigma_{xz}|^{m-1}\sigma_{xz}$, $w = u\partial_x b$.
- Boundary conditions at the free surface $z = H$, comprising of the non-stress conditions: $\sigma_{xz} = 0$, $p = 0$ and the kinematic condition: $\partial_t h + u\partial_x H = w$.

Eq. (4.2) results to a hydrostatic pressure which evolves linearly within the fluid: $p = H(x,t) - z$. Substituting this in Eq. (4.1) and integrating yields

$$\sigma_{xz} = (\lambda - \delta \partial_x H)(H - z). \tag{4.4}$$

This equation represents a balance between the shear stress and the pressure gradient together with gravity.

Following the approach by Boutounet et al. [2], in order to calculate the velocity profile the modulus of Eq. (4.4) can be obtained as

$$|\sigma_{xz}| = |\lambda - \delta\partial_x H|(H - z). \tag{4.5}$$

which implies that for a vanishing slope angle in the gravity term λ, the sign of the shear stress σ_{xz} remains the same as the sign of the local slope. A new variable Λ can thus be introduced using Eqs.(3.3) and (4.5) as

$$\Lambda = \begin{cases} \lambda & \text{for regime A,} \\ \lambda - \delta\partial_x H & \text{for regime B,} \end{cases} \tag{4.6}$$

regime A corresponding to the reference solution and regime B corresponding to the enriched regime containing an additional slope term $\delta\partial_x H$. As seen previously in the case of steady uniform flow, Eq. (4.4) shows that the evolution of shearing stress is linear indicating that there exist an unsheared (plug) zone near the surface of the flow as seen in Fig. 2(b), whose thickness h_p is obtained as

$$h_p = \frac{Bi}{\Lambda}. \tag{4.7}$$

This thickness, however, is not constant, it varies with the thickness gradient of the free surface, which implies existence of some elongational deformation in the plug. This contradicts the validity of lubrication approximation. To resolve this contradiction, a concept of pseudo-plug is introduced where the plug is made weakly sheared under the influence of normal stresses [5, 12, 13, 30].

Next, to obtain the depth-integrated law of mass conservation, the continuity equation is integrated from $z = b$ to $z = H$ applying Leibniz integral rule on the first term to get $\dfrac{\partial}{\partial x}\displaystyle\int_b^H u dz - u|_{z=H}\frac{\partial H}{\partial x} + u|_{z=b}\frac{\partial b}{\partial x} + \int_b^H dw = 0$. Taking $w|_{z=H} - w|_{z=b} = w|_{z=H}$ and applying the kinematic condition at the free surface recalling that the depth average velocity is defined as $\bar{u} = \frac{1}{h}\displaystyle\int_b^H u dz$, the depth-averaged mass conservation is obtained as

$$\frac{\partial h}{\partial t} + \frac{\partial (h\bar{u})}{\partial x} = 0. \tag{4.8}$$

To solve Eq. (4.8), the mean velocity $\bar{u}$ has to be determined by integrating the constitutive law (4.3) to obtain u. By substituting Eq. (4.4) and (4.7) into Eq. (4.3) and integrating, using the fact that $H = h_p + h_c + b$, equation of the velocity is obtained:

$$u(z) = \begin{cases} \Lambda|\Lambda|^{m-1}\left[\frac{1}{m+1}h_c^{m+1}\left(1 - \left(1 - \frac{z-b}{h_c}\right)^{m+1}\right) + Ch^m\right] & \text{if} \quad z < h_c + b, \\ \Lambda|\Lambda|^{m-1}\left[\frac{1}{m+1}h_c^{m+1} + Ch^m\right] & \text{if} \quad z \geq h_c + b. \end{cases} \tag{4.9}$$

The velocity component of the plug region is not constant, varies as soon as the slope changes, confirming the existence of some deformations as mentioned above. This velocity profile is locally identical to that of the zeroth-order solution of steady uniform flow, a perturbation of the reference flow.

Finally, to obtain an expression for the discharge rate $q = h\bar{u}$, u can be integrated to get

$$q = \Lambda|\Lambda|^{m-1}\left[h_c^{m+1}\left(\frac{1}{m+1}h_p + \frac{1}{m+2}h_c\right) + Ch^{m+1}\right]. \tag{4.10}$$

Inserting this expression into Eq. (4.8) the Lubrication type model (one-equation model) in variable h is

obtained:

$$\boxed{\frac{\partial h}{\partial t}+\frac{\partial}{\partial x}\left(\Lambda|\Lambda|^{m-1}\left[h_c^{m+1}\left(\frac{1}{m+1}h_p+\frac{1}{m+2}h_c\right)+Ch^{m+1}\right]\right)=0.} \tag{4.11}$$

For a Newtonian case when $Bi = 0$,and $m = 1$, the plug is absent, thus $H = h + b$ where $h = h_c$. The expression (4.9) simplifies to a quadratic velocity profile that depends on gravity and the slope: $u(z) = \Lambda\left[\frac{1}{2}h^2\left(1-\left(1-\frac{z-b}{h}\right)^2\right)+Ch\right]$. Thus the average velocity $\bar{u}$ in terms of thickness h becomes $\bar{u} = \Lambda\left(\frac{1}{3}h^2+Ch\right)$. Substituting this equation into the depth-integrated mass conservation (4.8), a simplified one-equation model of Benney's type with no surface tension term (see [7, 14]) is recovered: $\frac{\partial h}{\partial t}+\frac{\partial}{\partial x}\left(\Lambda\left(\frac{1}{3}h^2+Ch\right)h^3\right)=0$. To summarize, one advantage of lubrication approximation is that it reduces the primitive equations to a one non-linear diffusive equation governing the evolution of the fluid depth, which is less expensive to solve compared to the full Navier-Stokes equation. However, this model is over-simplified and may fail to capture all important flow details, for instance, the inertial terms are neglected at order zero. Researchers have also questioned the validity of lubrication approximation at high Reynolds number, and the associated error due to shallow layer assumption quantified, see [27]. This result has shown that, one equation type model is only valid for small aspect-ratio flows and can present singularities in finite time when linear stability threshold is exceeded, [19, 28]. The model is also not consistent with wet-dry front dynamics as $h \to 0$ [11, 14, 19]. The solution to these issues is to consider a two-equations model discussed in the next section, which is more consistent.

5 The Shallow Water type model (two-equations model)

The drawbacks of the one-equation model limit its validity to geophysical flows with complex rheology. This prompts us to consider a two-equations model otherwise known as the Shallow Water type model which is more complete and robust. The Shallow Water type model results from integration of the incompressible Navier-Stokes equations over the depth of the flow (this eliminates the vertical dimension) plus the shallow layer assumption $\epsilon << 1$.

Starting from the Navier-Stokes equations (2.1) and the associated boundary conditions, derivations are done following the work of [11, 12, 19]. Integration of the mass conservation expression over the depth was done in the previous section which is recalled here as the first equation model, see Eq. (4.11). Next, the momentum equation is also integrated over the fluid depth to obtain the second equation model. To achieve this, the x-momentum equation is integrated, and Leibniz integral rule applied together with the boundary conditions to give

$$\beta\left(\frac{\partial}{\partial t}\int_b^H u dz+\frac{\partial}{\partial x}\int_b^H u^2 dz\right)+\delta\frac{\partial}{\partial x}\int_b^H p dz=\epsilon^2\frac{\partial}{\partial x}\int_b^H \sigma_{xx}dz+\lambda h-\sigma_{xz}|_{z=b}-\left(\delta p|_{z=b}-\epsilon^2\sigma_{xx}|_{z=b}\right)\frac{\partial b}{\partial x}.$$

With some computations and introducing the flow rate $q = h\bar{u} = \int_b^H u dz$ and the shear stress at the base as $\sigma_{xz}|_{z=b} = \tau_b$ the second equation for Shallow Water type model in variables (h, q) is obtained as

$$\frac{\partial h\bar{u}}{\partial t}+\frac{\partial}{\partial x}\int_b^H u^2 dz-\frac{\alpha\delta}{\beta}\frac{\partial}{\partial x}\int_b^H \sigma_{xx}dz+\frac{\delta}{\beta}\frac{\partial}{\partial x}\int_b^H p dz+\frac{\delta}{\beta}\left(p|_{z=b}-\alpha\sigma_{xx}|_{z=b}\right)\frac{\partial b}{\partial x}=\frac{1}{\beta}\left(\lambda h-\tau_b\right). \tag{5.1}$$

To close the model, terms involving $\int_b^H u^2$, $\int_b^H \sigma_{xx}$, and $\int_b^H p$ need to be expressed in terms of h and $\bar{u}$ by asymptotic approximation. For geophysical flows such as lava flows with complex rheology, zeroth-order approximation is sufficient to describe the model. Order one, though more consistent, is more complex to implement for practicable use [11]. Thus, for the closure of the two-equations model, the following approximations at order zero are developed, following the approach of [11, 12]:

i. If assuming $u \approx \bar{u}$, the term involving $\int_b^H u^2 dz$ can be approximated as: $\int_b^H u^2 dz \approx h\bar{u}^2 = \frac{q^2}{h}$, which can be written as $\int_b^H u^2 dz = \frac{q^2}{h} +$ "the corrective term". Adopting the corrective term used in [11]: "corrective term"$= \frac{\Lambda^{2m} h^{2m+3}}{(2m+3)(m+2)^2}$, gives $\int_b^H u^2 dz \approx \int_b^H u^{(0)^2} dz = \frac{q^2}{h} + \frac{\Lambda^{2m} h^{2m+3}}{(2m+3)(m+2)^2}$. It is important to note that the corrective term vanishes as the slope Λ vanishes.

ii. The pressure term can be approximated from the zero-order expansion as: $\int_b^H p dz \simeq \int_b^H p^{(0)} dz = \frac{h^2}{2}$. Using this expression, the pressure terms in Eq. (5.1) can be added together as follows $\frac{\partial}{\partial x}\int_b^H p dz + p|_{z=b}\frac{\partial b}{\partial x} = \frac{\partial}{\partial x}\left(\frac{h^2}{2}\right) + h\frac{\partial b}{\partial x} = h\frac{\partial H}{\partial x}$.

iii. The terms in order $\frac{\alpha\delta}{\beta}$ are negligible, thus all terms in σ_{xx}can be dropped (as seen in Table 3, the weight coefficient $\frac{\alpha\delta}{\beta}$ is much smaller compared to others, hence can be neglected).

iv. The basal shear stress τ_b can be approximated at order zero as a function of flow rate, following the approach by [12]. From Eqs. (4.4) and (4.7) it can be written

$$\tau_b^{(0)} = \sigma_{xz}^{(0)}|_{z=b} = \Lambda\left(h_p + h_c\right). \tag{5.2}$$

This approximation is closed by expressing it in terms of the state variables h and q. Thus, by substituting the equivalent expression for Λ from Eq. (4.10) into Eq. (5.2) yields

$$\tau_b^{(0)} = |\Lambda|^{1-m}\left(h_p + h_c\right)\left[\frac{h\bar{u}}{h_c^{m+1}\left(\frac{1}{m+1}h_p + \frac{1}{m+2}h_c\right) + Ch^{m+1}}\right]. \tag{5.3}$$

In a similar way, Chambon [12] obtained a similar expression of the form

$$\tau_b = Bi + h_c\left[\frac{h\bar{u}}{h_c^{m+1}\left(\frac{1}{m+1}h_p + \frac{1}{m+2}h_c\right) + Ch^{m+1}}\right]^{\frac{1}{m}}. \tag{5.4}$$

The two-equations model (Shallow Water type) consists of the mass equation (4.8) and the momentum equation (5.1), providing a PDE system for the fluid height h and the discharge rate $h\bar{u}$. Applying the above approximations into Eq. (5.1), the two-equations system writes

$$\frac{\partial h}{\partial t} + \frac{\partial q}{\partial x} = 0, \quad \frac{\partial q}{\partial t} + \frac{\partial}{\partial x}\left(\frac{q^2}{h} + \frac{\Lambda^{2m} h^{2m+3}}{(2m+3)(m+2)^2}\right) + \frac{\delta}{\beta}h\frac{\partial H}{\partial x} = \frac{1}{\beta}\left(\lambda h - \tau_b\right), \tag{5.5}$$

with the basal shear stress τ_b written as

$$\tau_b = |\Lambda|^{1-m}\left(h_p + h_c\right)\frac{q}{D(h)}, \tag{5.6}$$

where the denominator $D(h)$ writes $D(h) = h_c^{m+1}\left(\frac{1}{m+1}h_p + \frac{1}{m+2}h_c\right) + Ch^{m+1}$.

Considering Newtonian case where $Bi = 0$ and $m = 1$, Eq. (5.6) reduces to: $\tau_b = \frac{3h^2\bar{u}}{h^3+3Ch^2}$. For a flat basal topography with no slip τ_b becomes $\tau_b = \frac{3\bar{u}}{h}$. This recovers, the two-equations model for a Newtonian fluid presented in [11, 14, 19]:

$$\frac{\partial h}{\partial t} + \frac{\partial q}{\partial x} = 0, \;\; \frac{\partial q}{\partial t} + \frac{\partial}{\partial x}\left(\frac{q^2}{h} + \frac{\delta}{2\beta}h^2 + \frac{\Lambda^2 h^5}{45}\right) = \frac{1}{\beta}\left(\lambda h - \frac{3q}{h^2}\right). \tag{5.7}$$

Similarly, setting $Bi > 0$ and $m = 1$ the Shallow Water model for Bingham fluids reported in [19] is recovered. Also, by setting $Bi = 0$ and $m \neq 1$ the Shallow Water model for power-law fluids presented in [11, 19] is recovered.

Using the dimensionless variables in Sec. 2.1 , the 1D two-equations model in physical form becomes

$$\frac{\partial h}{\partial t} + \frac{\partial q}{\partial x} = 0, \;\; \frac{\partial q}{\partial t} + \frac{\partial}{\partial x}\left(\frac{q^2}{h} + \frac{1}{2}gh^2\cos\theta + C_m\Lambda^{2m}h^{2m+3}\right) = gh\cos\theta\left(\tan\theta - \frac{\partial b}{\partial x}\right) - \frac{1}{\rho}\tau_b \tag{5.8}$$

where: $\tau_b = |\Lambda|^{1-m}K\left(h_p + h_c\right)\frac{q}{D(h)}$, $\Lambda = \frac{\rho g}{K}S_\theta$, with $S_\theta = \begin{cases} \sin\theta & \text{for regime A,} \\ \sin\theta - \cos\theta\frac{\partial H}{\partial x} & \text{for regime B,} \end{cases}$
the denominator $D(h) = h_c^{m+1}\left(\frac{1}{m+1}h - \frac{1}{(m+1)(m+2)}h_c\right) + C\left(h\right)^{m+1}$, $C_m = \frac{1}{(2m+3)(m+2)^2}$, the thickness of the sheared zone $h_c(z,t) = \max\left(0, h(z,t) - h_p(z,t)\right)$, the plug thickness $h_p(z,t) = \frac{\tau_c}{\rho g S_\theta}$.

An important remark is that the Shallow Water model is closed when all terms are expressed in terms of averaged velocity and depth. Accordingly, the slope can be expressed as $\tan\theta = -\frac{\partial h}{\partial x}$, with the negative sign indicating the direction of the flow.

To extend the derivations to two dimensions, the Shallow Water system is derived from the integration of the 3D incompressible Navier-Stokes equations (5.9). For the purpose of derivation, a configuration in which either x or y is the axis of the slope at an angle θ with z being the axis normal to the slope is considered

$$\begin{aligned}
&\beta(\partial_t u + u\partial_x u + v\partial_y u + w\partial_z u) = -\delta\partial_x p + \lambda_x + \alpha\delta\left(\partial_x\sigma_{xx} + \partial_y\sigma_{xy}\right) + \partial_z\sigma_{xz}, \\
&\beta(\partial_t v + u\partial_x v + v\partial_y v + w\partial_z v) = -\delta\partial_y p + \lambda_y + \alpha\delta\left(\partial_x\sigma_{xy} + \partial_y\sigma_{yy}\right) + \partial_z\sigma_{yz}, \\
&\epsilon^2\beta(\partial_t w + u\partial_x w + v\partial_y w + w\partial_z w) = -\delta(\partial_z p + 1) + \alpha\delta(\partial_x\sigma_{xz} + \partial_y\sigma_{yz} + \partial_z\sigma_{zz}).
\end{aligned} \tag{5.9}$$

Considering 0^{th} order terms in ϵ and assuming $\beta = \alpha = O(\epsilon)$, the governing equations reduces to the following system of equations:

- Conservation of mass: $\partial_x u + \partial_x u + \partial_z w = 0$.
- Conservation of momentum:

$$\partial_z\sigma_{xz} = \delta\partial_x p - \lambda_x, \tag{5.10}$$

$$\partial_z\sigma_{yz} = \delta\partial_y p - \lambda_y, \tag{5.11}$$

$$\partial_z p = -1. \tag{5.12}$$

- Herschel-Bulkley rheology law introduced in Section 2.1 reduces to

$$\begin{cases} \sigma_{xz} = \left(\frac{Bi}{\dot{\gamma}} + \dot{\gamma}^{n-1}\right)\partial_z u, & \\ \sigma_{yz} = \left(\frac{Bi}{\dot{\gamma}} + \dot{\gamma}^{n-1}\right)\partial_z v, & \text{if} \quad \tau > Bi, \\ \dot{\gamma}_{ij} = 0 & \text{if} \quad \tau \leq Bi, \end{cases} \tag{5.13}$$

  where the deformation tensor norm: $\dot{\gamma} = \sqrt{(\partial_z u)^2 + (\partial_z v)^2}$ and the stress norm:

$$\tau = \sqrt{\sigma_{xz}^2 + \sigma_{yz}^2}. \tag{5.14}$$

- Friction condition: $u = C|\sigma_{xz}|^{m-1}\sigma_{xz}$, $v = C|\sigma_{yz}|^{m-1}\sigma_{yz}$ and $w = u\partial_x b + v\partial_y b$, at the bottom $z = b$. When $C = 0$ the no-slip condition is recovered.

- Non-stress conditions: $\sigma_{xz} = \sigma_{yz} = 0$, $p = 0$, and kinematic condition: $\partial_t h + u\partial_x H + v\partial_y H = w$, at the free surface $z = H$.

Integrating Eq. (5.12) a hydrostatic pressure with a linear evolution is obtained: $p = H(x, y, t) - z$. Substituting this in Eq. (5.10) and (5.11) and integrating, results to

$$\sigma_{xz} = \Lambda_x(H - z), \quad \sigma_{yz} = \Lambda_y(H - z), \tag{5.15}$$

where, if x is considered as the axis of the slope, y as the horizontal axis and z the normal axis to the slope, Λ defined in Section 4 writes

$$\Lambda = \lambda\tbinom{1}{0} \text{ for regime A}, \quad \Lambda = \lambda\tbinom{1}{0} - \delta\tbinom{\partial_x H}{\partial_y H} \text{ for regime B}. \tag{5.16}$$

Otherwise, when considering a general case in which the axis of the slope is either x or y, the gravity term can be written as

$$\Lambda = \lambda\tbinom{1}{1} \text{ for regime A}, \quad \Lambda = \lambda\tbinom{1}{1} - \delta\tbinom{\partial_x H}{\partial_y H} \text{ for regime B}. \tag{5.17}$$

Eq. (5.14) can now be written in terms of Λ as

$$\tau = \sqrt{\left(\Lambda_x^2 + \Lambda_y^2\right)}(H - z). \tag{5.18}$$

On the yield surface: $h = h_c$ and $\tau = Bi$, thus the thickness of the sheared zone is obtained as

$$h_c = h - \frac{Bi}{||\Lambda||} \qquad \text{for} \quad \tau > Bi, \tag{5.19}$$

which in general, writes: $h_c = \max(0, h - h_p)$, where the plug thickness $h_p = \frac{Bi}{||\Lambda||}$ and $||\Lambda|| = \sqrt{\left(\Lambda_x^2 + \Lambda_y^2\right)}$.

Next, from the rheology law (5.13), τ can be written as

$$\tau = \sqrt{\sigma_{xz}^2 + \sigma_{yz}^2} = Bi + \dot{\gamma}^n. \tag{5.20}$$

Note that Eq. (5.18) and Eq. (5.20) are equivalent, which after a few arrangements translates to

$$\partial_z u = \Lambda_x (h_c + b - z)^{\frac{1}{n}}, \;\; \partial_z v = \Lambda_y (h_c + b - z)^{\frac{1}{n}} \tag{5.21}$$

in x- and y-direction, respectively. Integrating these expressions and applying the friction condition, the velocity distribution in the x- and y-direction respectively, is obtained:

$$\begin{aligned} u(z) &= \begin{cases} \Lambda_x |\Lambda_x|^{m-1} \left[\frac{1}{m+1} \left(h_c^{m+1} - (h_c - z - b)^{m+1} \right) + C h^m \right] & \text{if} \quad z < h_c, \\ \Lambda_x |\Lambda_x|^{m-1} \left[\frac{1}{m+1} h_c^{m+1} + C h^m \right] & \text{if} \quad z \geq h_c. \end{cases} \\ v(z) &= \begin{cases} \Lambda_y |\Lambda_y|^{m-1} \left[\frac{1}{m+1} \left(h_c^{m+1} - (h_c - z - b)^{m+1} \right) + C h^m \right] & \text{if} \quad z < h_c, \\ \Lambda_y |\Lambda_y|^{m-1} \left[\frac{1}{m+1} h_c^{m+1} + C h^m \right] & \text{if} \quad z \geq h_c. \end{cases} \end{aligned} \tag{5.22}$$

The flow rate in both directions can be calculated by integrating $q_x = h\bar{u} = \int_b^H u dz$ and $q_y = h\bar{v} = \int_b^H v dz$ respectively to obtain

$$\begin{aligned} q_x &= \Lambda_x |\Lambda_x|^{m-1} \left[h_c^{m+1} \left(\frac{1}{m+1} h_p + \frac{1}{m+2} h_c \right) + C h^{m+1} \right], \\ q_y &= \Lambda_y |\Lambda_y|^{m-1} \left[h_c^{m+1} \left(\frac{1}{m+1} h_p + \frac{1}{m+2} h_c \right) + C h^{m+1} \right]. \end{aligned} \tag{5.23}$$

The first equation of the model (lubrication type) can now be written in 2D:

$$\boxed{\frac{\partial h}{\partial t} + \frac{\partial q_x}{\partial x} + \frac{\partial q_y}{\partial y} = 0.} \tag{5.24}$$

To obtain the second equation of the model, following the approach presented for 1D case, the x- and y-momentum equations are integrated over the fluid depth, applying Leibniz integral rule and the boundary conditions to obtain:
the x-component:

$$\begin{aligned} \frac{\partial h\bar{u}}{\partial t} + \frac{\partial}{\partial x} \int_b^H u^2 dz + \frac{\partial}{\partial y} \int_b^H uv dz - \frac{\alpha\delta}{\beta} \left(\frac{\partial}{\partial x} \int_b^H \sigma_{xx} dz + \frac{\partial}{\partial y} \int_b^H \sigma_{xy} dz + \sigma_{xy}|_{z=b} \frac{\partial b}{\partial y} - \sigma_{xy}|_{z=H} \frac{\partial H}{\partial y} \right) \\ + \frac{\delta}{\beta} \frac{\partial}{\partial x} \int_b^H p dz + \frac{\delta}{\beta} \left(p|_{z=b} - \alpha \sigma_{xx}|_{z=b} \right) \frac{\partial b}{\partial x} = \frac{1}{\beta} \left(\lambda_x h - \tau_{b_x} \right), \end{aligned}$$

the y-component:

$$\begin{aligned} \frac{\partial h\bar{v}}{\partial t} + \frac{\partial}{\partial x} \int_b^H uv dz + \frac{\partial}{\partial y} \int_b^H v^2 dz - \frac{\alpha\delta}{\beta} \left(\frac{\partial}{\partial x} \int_b^H \sigma_{xy} dz + \frac{\partial}{\partial y} \int_b^H \sigma_{yy} dz + \sigma_{xy}|_{z=b} \frac{\partial b}{\partial x} - \sigma_{xy}|_{z=H} \frac{\partial H}{\partial x} \right) \\ + \frac{\delta}{\beta} \frac{\partial}{\partial y} \int_b^H p dz + \frac{\delta}{\beta} \left(p|_{z=b} - \alpha \sigma_{yy}|_{z=b} \right) \frac{\partial b}{\partial y} = \frac{1}{\beta} \left(\lambda_y h - \tau_{b_y} \right). \end{aligned}$$

Considering both directions, the zeroth-order approximations defined at the begining of this section can now

be used to close the model. This yields the two-equations model in 2D:

$$\begin{aligned}
&\frac{\partial h}{\partial t}+\frac{\partial h\bar{u}}{\partial x}+\frac{\partial h\bar{v}}{\partial y}=0,\\
&\frac{\partial h\bar{u}}{\partial t}+\frac{\partial}{\partial x}\left(h\bar{u}^2+\frac{\delta}{2\beta}h^2+C_m\Lambda_x^{2m}h^{2m+3}\right)+\frac{\partial}{\partial y}(h\bar{u}\bar{v}+C_m\Lambda_y^{2m}h^{2m+3})=\frac{1}{\beta}\left(\lambda_x h-\delta h\frac{\partial b}{\partial x}-\tau_{b_x}\right),\\
&\frac{\partial h\bar{v}}{\partial t}+\frac{\partial}{\partial x}\left(h\bar{u}\bar{v}+C_m\Lambda_x^{2m}h^{2m+3}\right)+\frac{\partial}{\partial y}\left(h\bar{v}^2+\frac{\delta}{2\beta}h^2+C_m\Lambda_y^{2m}h^{2m+3}\right)=\frac{1}{\beta}\left(\lambda_y h-\delta h\frac{\partial b}{\partial y}-\tau_{b_y}\right),
\end{aligned}\tag{5.25}$$

with basal shear stress components approximated at order zero from Eq. (5.15), which after substituting Eq. (5.23) for Λ in both directions, yields

$$\tau_{b_x}=|\Lambda_x|^{1-m}\left(\frac{Bi}{||\Lambda||}+h_c\right)\frac{q_x}{D(h)},\quad \tau_{b_y}=|\Lambda_y|^{1-m}\left(\frac{Bi}{||\Lambda||}+h_c\right)\frac{q_y}{D(h)},\tag{5.26}$$

where the denominator $D(h)=h_c^{m+1}\left(\frac{1}{m+1}h-\frac{1}{(m+1)(m+2)}h_c\right)+Ch^{m+1}$ and $C_m=\frac{1}{(2m+3)(m+2)^2}$.

In dimensional form the two-equations model in 2D writes

$$\boxed{\begin{aligned}
&\frac{\partial h}{\partial t}+\frac{\partial q_x}{\partial x}+\frac{\partial q_y}{\partial y}=0,\\
&\frac{\partial q_x}{\partial t}+\frac{\partial}{\partial x}\left(\frac{q_x^2}{h}+\frac{1}{2}gh^2\cos\theta+C_m\Lambda_x^{2m}h^{2m+3}\right)+\frac{\partial}{\partial y}\left(\frac{q_xq_y}{h}+C_m\Lambda_y^{2m}h^{2m+3}\right)=-hg\cos\theta\frac{\partial H}{\partial x}-\frac{1}{\rho}\tau_{b_x},\\
&\frac{\partial q_y}{\partial t}+\frac{\partial}{\partial x}\left(\frac{q_xq_y}{h}+C_m\Lambda_x^{2m}h^{2m+3}\right)+\frac{\partial}{\partial y}\left(\frac{q_y^2}{h}+\frac{1}{2}gh^2\cos\theta+C_m\Lambda_y^{2m}h^{2m+3}\right)=-hg\cos\theta\frac{\partial H}{\partial y}-\frac{1}{\rho}\tau_{b_y},
\end{aligned}}\tag{5.27}$$

where $\Lambda=\frac{\rho g}{K}S_\theta$, with $S_\theta=\sin\theta\begin{pmatrix}1\\0\end{pmatrix}$ for regime A, or $S_\theta=\sin\theta\begin{pmatrix}1\\0\end{pmatrix}-\cos\theta\begin{pmatrix}\partial_x H\\ \partial_y H\end{pmatrix}$ for regime B. The basal shear stress is expressed as

$$\boldsymbol{\tau}_b=\begin{bmatrix}\tau_{b_x}\\ \tau_{b_y}\end{bmatrix}=\begin{bmatrix}K\left(\frac{K}{\rho g|S_{\theta_x}|}\right)^{m-1}\left(\frac{\tau_c}{\rho g||S_\theta||}+h_c\right)\frac{q_x}{D(h)}\\ K\left(\frac{K}{\rho g|S_{\theta_y}|}\right)^{m-1}\left(\frac{\tau_c}{\rho g||S_\theta||}+h_c\right)\frac{q_y}{D(h)}\end{bmatrix},\tag{5.28}$$

where as presented previously, the sheared thickness $h_c=\max(0,h-h_p)$ and the plug thickness $h_p=\frac{\tau_c}{\rho g||S_\theta||}$, as seen in Fig. 2. By setting $\tau_c=0$, $m=1$ and $\theta=0$**,** the classical Shallow Water equation**s** for Newtonian flows are recovered.

6 Numerical results

This section presents computed results of a few cases considered using the Shallow Water equations 5.27. To start with, numerical results are compared with experimental results for validation. Thereafter, steady-state flows with a bump at the center are considered for analysis. Results are computed using COMSOL multiphysics applying the "Shallow Water equations interface" and DassFlow open-source software [26] for cross-validation. COMSOL multiphysics employs a first order Discontinuous Galerkin scheme in space and Runge-Kutta in time. DassFlow employs demonstrated robust Finite Volume (FV) schemes (both first and

second order), see [17, 25, 32] in the Newtonian case. For the present Herschel-Buckley case, the first order FV scheme has been enriched; details are presented in the appendix. Results presented are for Regime A (using both Comsol and DassFlow) unless stated otherwise while comparing with Regime B (using Comsol only).

6.1 Validation

To test the accuracy and reliability of the Shallow Water equations model to predicting actual behavior of the fluid flow, computed results are compared with experimental results presented in [15,16] and [29]. Two cases are considered: flows on an inclined surface and on a horizontal surface with a topography. Experimental data is extracted from the literature using WebPlotDigitize free online software with an estimated error margin of less than 0.05 [34].

6.1.1 Dam-break experiment on an inclined surface

To validate the numerical model on an inclined surface, a dam-break experiment of [15, 16] is considered. The experiment involves the sudden release of fixed volumes of a viscoplastic fluid down a plane inclined at some angle θ, as seen in Fig. 3. The fluid is initially locked in a reservoir set at the top of the plane before

(a) (b)

Figure 3: Dam-break geometry: (a) Side-view (b) top-view of the geometry.

it is released suddenly by opening the lock gate. Data used is obtained from [3, 15, 16]: inclination $\theta = 12^o$, density $\rho = 1000kg/m^3$, rheological information of Carbopol ultrez 10 for different concentrations as shown in Table 3, and an initial fluid height 0.36m. The reservoir is of length $0.51m$ and width $0.3m$, while the plane is of length $4m$ and width $1.2m$.

Concentration	0.25%	0.3%	0.35%
$K(Pa\,s^n)$	32.1	47.7	58.9
n	0.39	0.42	0.51
$\tau_c(Pa)$	78	89	102

Table 3: Rheological details of Carbopol ultrez 10 used. Data obtained from [3, 15, 16].

The wall condition (with $C = 0$) is used on all boundaries. Unless stated otherwise, simulations are carried out using 43kg of Carbopol ultrez 10 at a concentration of 0.3%. An unstructured mesh with 2000 number of elements is used for discretization with a time-step $\Delta t = 0.05$.

Fig. 4 shows computed results plotted against experimental results. The front positions varying with time for 0.3% and 0.25% concentration of Carbopol ultrez 10 on a slope of $\theta = 12^o$ and $\theta = 18^o$ are shown.

Simulation results are in good agreement with experimental results. A small difference is observed, especially at early times after releasing the fluid. This discrepancy could be attributed to the experimental errors reported in the literature. For instance, it was reported that the dam-gate took some time to fully open

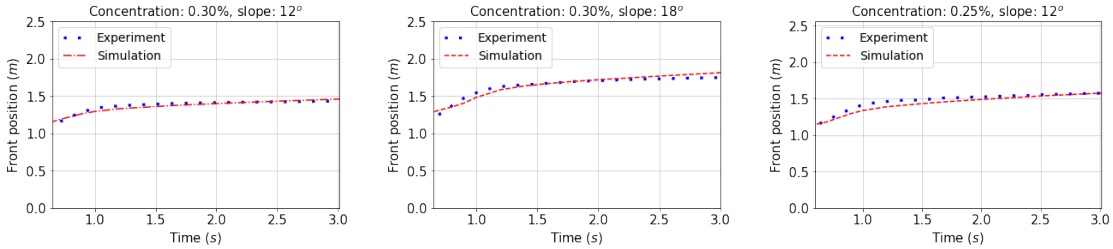

(a) (b) (c)

Figure 4: Comparing experimental and simulation results of a dam-break problem: front positions varying with time for 0.3% concentration of Carbopol ultrez 10 on a slope of $\theta = 12^o$ (a), $\theta = 18^o$ (b), and for 0.25% concentration on a slope of $\theta = 12^o$(c).

while in simulations the gate is assumed to open instantly releasing the whole bulk of the fluid instantaneously. Moreover, at the initial stage of the flow (where $\epsilon \simeq 0.6$), this dam-break problem is not compatible with the shallow flow assumption (as it does not obey the thin-layer assumption $\epsilon << 1$). (Similar observations are reported e.g. in [8]).

Fig. 5(a) shows the evolution of fluid height with time of a Herschel-Bulkley fluid for various time instants.

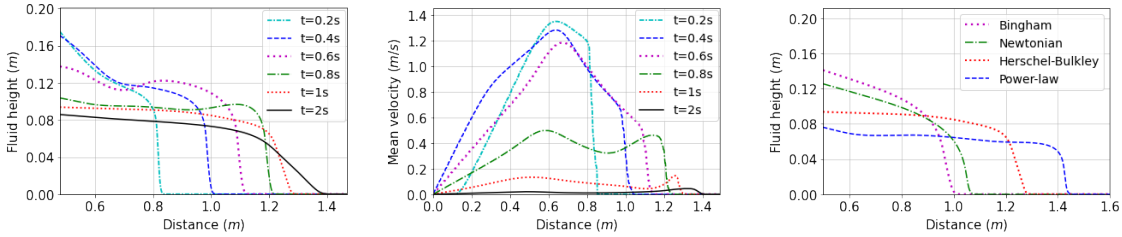

(a) (b) (c)

Figure 5: Fluid evolution in a dam-break problem: (a) fluid height evolution at different time instants, (b) mean velocity at different time instants, (c) fluid depth at $t = 1s$ for various fluid types.

The corresponding mean velocity is plotted in Fig. 5(a). The fluid propagates as expected with the flow front advancing in time. Both fluid thickness and mean velocity are reducing in time as the flow front spreads further. Fig. 5(c) shows the comparison of fluid heights for a Newtonian, Herschel-Bulkley and power-law fluid respectively at $t = 1s$. Bingham fluid is obtained by setting $n = 1$, power-law fluid by setting $\tau_c = 0Pa$ and Newtonian fluid achieved by setting $\tau_c = 0Pa$ and $n = 1$, while keeping other parameters constant. Having used the same consitency index, it is observed that the power-law fluid spreads faster than the Herschel-Bulkley which spreads faster than the Newtonian fluid. For 2D visualization, computed flow

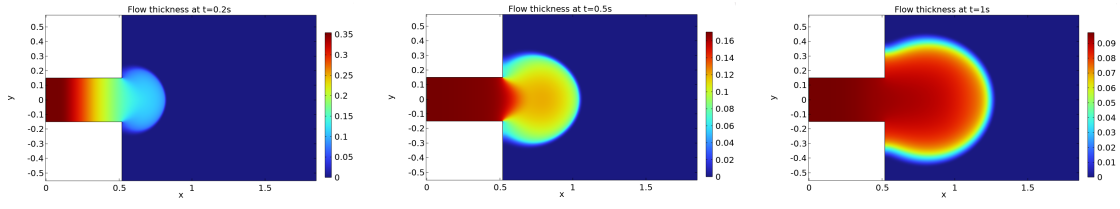

(a) (b) (c)

Figure 6: 2D visualization of the dam-break flow for different time instants

thickness at $t = 0.2$s, $t = 0.5$s and $t = 1$s respectively is shown in Figure 6. The fluid advances in both

directions past the reservoir gate as expected. The height is observed from the color legends on the right, to reduce with time as the fluid flows. These results confirm the ability of the Shallow Water model to well simulate these 3D flows.

6.1.2 Dam-break experiment on a horizontal surface with a topography

To validate the numerical model on a horizontal surface with a topography, a dam-break experiment done by [29] is considered. This experiment was carried out using water on a rectangular horizontal channel of length $8.9m$ and width $0.3m$. A reservoir of width $0.3m$ was set $4.65m$ from the channel entrance, see Fig. 3(a), with angle $\theta = 0^o$. The reservoir was initially filled with $0.25m$ of water at rest. A trapezoidal shaped topography of base length $1m$, top length $0.3m$ and height $0.075m$ is located $6.18m$ downstream from the entrance. The reservoir gate is opened suddenly and surface elevation data captured using video cameras.

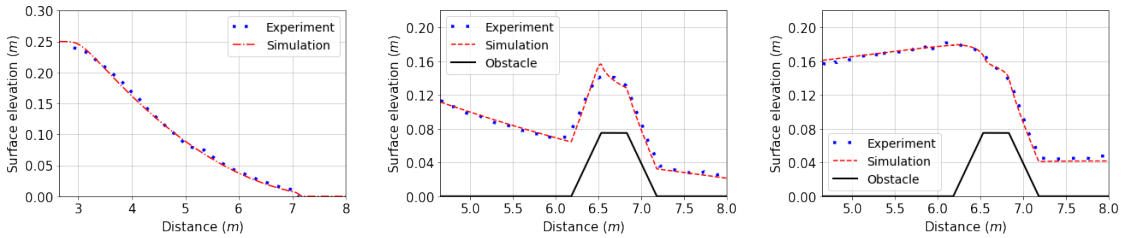

(a) (b) (c)

Figure 7: Comparing experimental and simulation results of a dam-break problem for Newtonian case. Free surface profile on a flat surface (a) and over a topography at $t = 1.9s$ (b) and $t = 6.6s$ (c).

For numerical simulations, an unstructured mesh with 2000 number of elements is used for discretization with a time-step $\Delta t = 0.05$. The wall condition (with $C = 0$) is used on all boundaries. Computed free surface profiles are compared with experimental data with and without a topography at $t = 1s$, $t = 1.9s$ and $t = 6.6s$ respectively, as seen in Fig. 7. Numerical results are achieved using a Newtonian fluid for regime B by setting $\tau_c = 0Pa$ and $n = 1$ and $K = 0.001Pa\,s^n$. Experimental results are accurately predicted by numerical results with or without a topography. This confirms the reliability of the model to simulating unsteady flows over topography. It is worth noting that the long-wave assumption is obeyed in this test case with $\epsilon \simeq 0.05$ at the initial stage.

6.2 Steady flow with a bump at the center

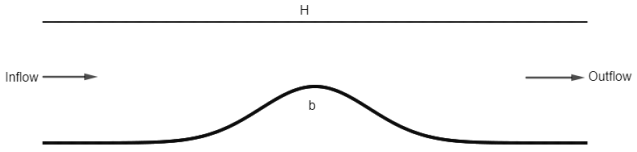

Figure 8: Flow geometry on a flat topography with a bump at the center

In this subsection, a steady state flow on a flat topography with a bump at the center is considered, as shown in Fig. 8. The topography given by $b(x) = 0.5e^{-0.5(\frac{2x-L}{2})^2}$is set on a domain such that $0 \leq x \leq L$

where $L = 10m$. The same data described as in Table 3 for 0.3% concentration of Carbopol ultrez 10 is used together with a density $\rho = 1000Kg/m^3$ and inclination $\theta = 12^o$. To mimic a real-like consistency index that is temperature dependent, a consistency index that varies linearly with time is set such that: $K = \left(\frac{K_f - K_o}{t_f}\right) t + K_o$ where consistency index at initial time t_o is $K_o = 30Pa\,s^n$ and at some final time t_o is $K_f = 60Pa\,s^n$. These values are chosen arbitrary from Table 3. An unstructured mesh with 2000 quadrilateral elements is used for discretization with $\Delta t = 0.05$. The aspect ratio is estimated as $\epsilon = H/L \simeq 0.1$ from which dimensionless numbers defined in Section 2.1 are locally computed with time. To ensure a steady-state is achieved, the iterations are run until the relative error between solutions of two consecutive time steps is below the stationarization tolerance: $\frac{|h^{n+1} - h^n|}{|h^n|} < 10^{-3}$.

6.2.1 Steady uniform flow

To achieve a steady uniform flow, the following conditions are imposed: initial fluid elevation $H(x,0) = h(x,0) + b(x) = 0.5m$ and a mean velocity value $\bar{u}(x,0) = 3.125cm/s$, uniform Dirichlet boundary conditions: $h(x,0) = 1.0m$ and $\bar{u} = 6.25cm/s$ at both inlet and outlet, and a wall condition at the bottom (with $C = 0$).

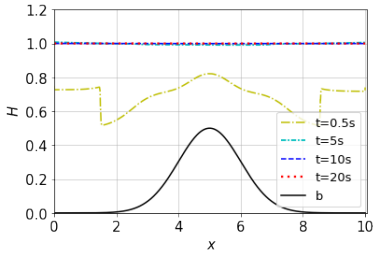

Figure 9: Time evolution of the fluid elevation. A steady state is reached at $t = 10s$ with a tolerance of about 10^{-8}.

As expected for a uniform steady state flow, the fluid elevation attains a constant steady value at about $t = 10s$ as seen in Fig. 9 with a steady state tolerance of less than 10^{-8}. Similarly, for dimensionless numbers in Fig. 10, a steady state is achieved at $t = 10s$.

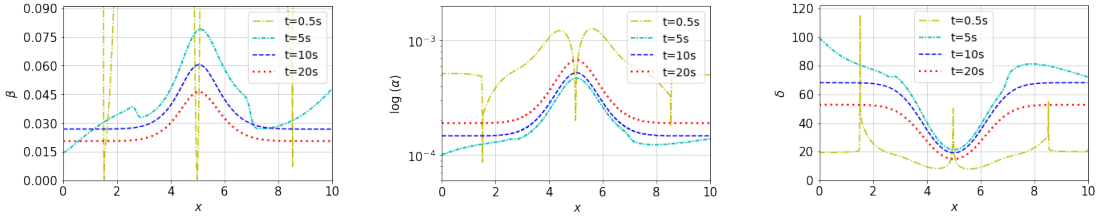

(a) (b) (c)

Figure 10: Time evolution of dimensionless numbers: β, α and δ respectively. Convergence for dimensionless numbers is not expected since consistency index K varies with time.

Dimensionless parameters: β, α and δ, defined in Section 2.1 are plotted in Fig. 10 for different time instants using local values. The weight coefficient β in Fig.10 (a) corresponding to inertial term is maximum at initial time $t = 0.5$s when the flow is unsteady with high Reynolds number and reduces with time as the flow becomes steady. The viscous term coefficient α in (b) increases with time as the flow achieves steady

state. Similarly, as seen in (c) the pressure term coefficient δ becomes steady with time as the flow progresses. There is high pressure at the initial stage which becomes steady with time.

To study the difference between the two flow regimes, the gravity term defined in Section 4 in is normalized as

$$\frac{\Lambda}{\lambda} = \begin{cases} 1 & \text{for regime A,} \\ 1 - \frac{\delta}{\lambda}\partial_x H & \text{for regime B,} \end{cases} \tag{6.1}$$

from which, a regime correction criterion differentiating the two regimes can be defined as $\frac{\delta}{\lambda}\partial_x H$. In physical dimensions $\frac{\delta}{\lambda}$=cotθ and $\lambda = \frac{\rho g}{K}$. Time evolution of this term is plotted in Fig. 11. Regime A is represented

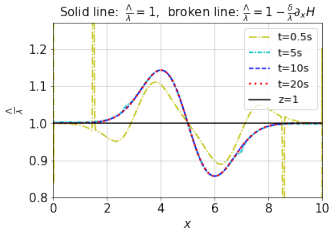

Figure 11: Time evolution of the normalized gravity term $\frac{\Lambda}{\lambda}$.

by line $\frac{\Lambda}{\lambda} = 1$ while regime B enriched with the correction term ($\frac{\delta}{\lambda}\partial_x H$) is represented by $\frac{\Lambda}{\lambda} = 1 - \frac{\delta}{\lambda}\partial_x H$. Equilibrium state is reached at $t = 10$s. The difference is approximately 15% around the bump on both sides of the mean position and negligible everywhere else. This clearly depicts that a deviation between the two regimes only occurs when there is a change in slope within the flow e.g. due to varying topographies. However, this difference does not manifest itself within the state variables. This is noticed while comparing H and U at time $t = 10s$ between the two regimes, with a very small relative difference of about $\frac{|h_B - h_A|}{|h_A|} < 10^{-5}$ observed. This shows that a 15% disparity observed within the normalized gravity term corresponds to a $< 10^{-3}$% difference within the state variables, which has insignificant effects on the flow. This concludes that the corrective term ($\frac{\delta}{\lambda}\partial_x H$) can be neglected in steady uniform laminar flows (unless its magnitude is large enough to cause observable perturbations of course).

6.2.2 Steady non-uniform flow

To achieve a steady non-uniform flow, similar conditions for initial data are used: i.e. fluid height $H(x,0) = h(x,0) + b(x) = 0.5m$, a mean velocity value $\bar{u}(x,0) = 3.125cm/s$, wall condition at the bottom (i.e. no-flux condition with $C = 0$), inlet boundary conditions: $q = 6.25cm/s$ (with $h = 1.0m$) and the outlet is left open to allow transmission from the domain values. A steady state is reached at $t = 10s$ with a stationarization tolerance of about 10^{-6}. Fig. 12 shows evolution of fluid elevation in time over a bump for various time instants, with a shock evidently observed around point $x = 6$m. The flow is non-uniform with a sharp change of slope at the top of the bump. Strict convergence to a steady-state is not expected as the consistency index is set to vary linearly with time from low viscosity to a relatively high viscosity.

Fig. 13 shows dimensionless parameters evolving in time. The discussion is the same as for the steady uniform case; with β and δ reducing with time as the fluid reaches equilibrium. On the other hand, α varies inversely increasing with time as the flow attains steady-state as expected.

Fig. 14 shows the normalized gravity term given by Eq. 6.1 evolving in time. A regime correction criterion

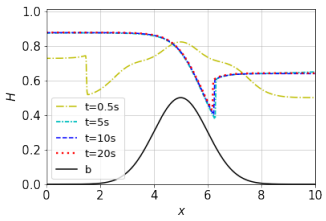

Figure 12: Time evolution of the fluid elevation. A steady state is observed at $t = 10s$ with a tolerance of about 10^{-6}.

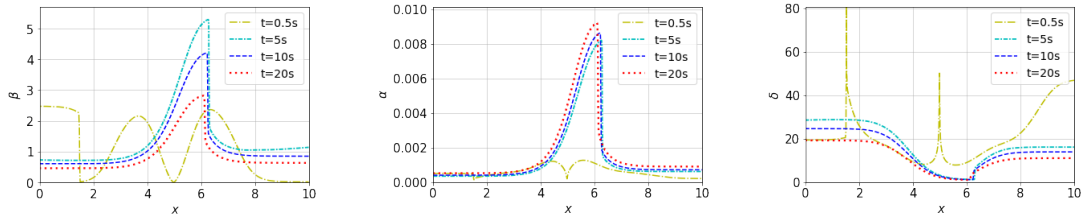

(a) (b) (c)

Figure 13: Time evolution of dimensionless numbers: β, α and δ respectively. Convergence for dimensionless numbers is not expected since consistency index (mimicking real-like lava viscosity) varies with time.

of about 18% can be observed on the left hand side of the bump in Fig. 14(a), and about 500% after the tip of the bump on the right hand side where the shock is observed, see Fig. 14(b). This clearly depicts that a sharp change of slope increases the magnitude of the corrective term where a perturbation on the flow is expected.

Fig. 15 shows the difference between the two regimes for the state variables: H and U respectively, and Froude number Fr, plotted in both COMSOL and DassFlow simulation softwares for cross-comparison. There is agreement between the two codes as observed for regime A. The difference between regime A and B, however is clearly observed where the gradient is changing sharply i.e. around position $5.0 - 7.0$ in $x-$values. The maximum relative difference between the two regimes at about $x = 6.2$m can be computed as $\frac{|h_B - h_A|}{|h_A|} \approx 0.3$m. However, this disparity is negligible everywhere else beyond the point where the gradient is changing, as also seen in the previous case of a steady uniform state. These results have shown that the corrective term in regime B improves solution in areas with a very sharp change of slope, otherwise negligible everywhere else.

7 Conclusion

This paper presents derivations of thin-layer flow models: 2D lubrication and Shallow Water equations, valid for multi-regime flows of viscoplastic Herschel-Bulkley fluids on inclined non-flat topographies. From the primitive Navier-Stokes equations with free-surface and friction-law condition, these models are derived by asymptotic expansion method, extending the work of [11, 12, 28] to 3D multi-regime flows with varying basal conditions. Starting from zeroth-order solutions, flow models and the corresponding flow regimes are calculated. Classical reference solutions in the literature are recovered by considering particular cases on flat topographies. Numerical solutions of the Shallow Water equations are obtained using both a Finite Volume solver implemented into the open source computational software DassFlow [26] and a Discontinuous Galerkin scheme implemented into the commercial software COMSOL multiphysics [31], for cross-validations.

(a) (b)

Figure 14: Time evolution of the normalized gravity term $\frac{\Lambda}{\lambda}$: (a) the y-axis values ranges from 0.6 - 1.2 to while (b) ranges from -4.0 - 1.0 to view the lower side of the mean position $\frac{\Lambda}{\lambda}=1$

(a) (b)

Figure 15: Comparing fluid elevation H (a) and mean velocity U (b) for regime A and B at $t=10s$. The difference between the two regimes is evident where the slope is changing.

Numerical results are compared with dam-break experiments presented in [15, 16] on an inclined plane, and in [29] on a horizontal surface with varying topography. A good agreement between experimental and numerical results is achieved, which confirms the ability of the numerical model to simulate complex fluid flows. The two flow regimes (the standard one, Regime A and the less classical one, Regime B) corresponding to different balances between shear and pressure forces are numerically analyzed and compared. Two steady state cases (uniform and non-uniform) are studied to investigate the difference between the two regimes within the flow fields. Differences are observed in high slope areas within non-uniform flows. This shows that the additional term present in the enriched equations modeling Regime B enables more consistent approximation of flows in the vicinity of sharp slope variations. The numerical models which have been derived are able to simulate real-world flows presenting Herschel-Bulkley rheology like lava flows.

Declaration of competing interest

The authors declare that they have no known competing financial interests or personal relationships that could have appeared to influence the work reported in this paper

Acknowledgments & authors' contributions

Authors would like to thank the Royal Society of New Zealand through the Marsden grant UOC1802 for providing funds to do this research towards completion of the first author's PhD studies.
The first author has derived the equations and built up the computational methods from the previous studies which are mentioned here, under the guidance of the corresponding author. The first author has performed all the numerical results; he has enriched the computational software DassFlow2D from the previous version which was considering the Newtonian case only. The last author, P.I. of this multidisciplinary Marsden project, has supervised the first author on the use of COMSOL and results analysis.

The authors warmly acknowledge Prof. J.-P. Vila from INSA - Math Institute of Toulouse for having introduced the corresponding author to these model derivations and G. Chambon for providing his rich Habilitation thesis document.

References

[1] C. Acary-Robert, E. D. Fernández-Nieto, G. Narbona-Reina, and P. Vigneaux. A well-balanced Finite Volume-augmented lagrangian method for an integrated Herschel-Bulkley model. *Journal of Scientific Computing*, 53:608–641, 2012.

[2] C. Ancey. Plasticity and geophysical flows: a review. *Journal of Non-Newtonian Fluid Mechanics*, 142:4–35, 2007.

[3] C. Ancey and S. Cochard. The dam-break problem for Herschel–Bulkley viscoplastic fluids down steep flumes. *Journal of Non-Newtonian Fluid Mechanics*, 158:18–35, 2009.

[4] E. Audusse, F. Bouchut, M.-O. Bristeau, R. Klein, and B. T. Perthame. A fast and stable well-balanced scheme with hydrostatic reconstruction for Shallow Water flows. *SIAM Journal on Scientific Computing*, 25:2050–2065, 2004.

[5] N. Balmforth and R. Craster. A consistent thin-layer theory for Bingham plastics. *Journal of Non-Newtonian fluid mechanics*, 84:65–81, 1999.

[6] N. J. Balmforth, R. V. Craster, A. C. Rust, and R. Sassi. Viscoplastic flow over an inclined surface. *Journal of Non-Newtonian Fluid Mechanics*, 139:103–127, 2006.

[7] D. Benney. Long waves on liquid films. *Journal of Mathematics and Physics*, 45:150–155, 1966.

[8] N. Bernabeu, P. Saramito, and C. Smutek. Numerical modeling of non-Newtonian viscoplastic flows: Part II. viscoplastic fluids and general tridimensional topographies. *International Journal of Numerical Analysis and Modeling*, 11:213–228, 2014.

[9] N. Bernabeu, P. Saramito, and C. Smutek. Modelling lava flow advance using a shallow-depth approximation for three-dimensional cooling of viscoplastic flows. *Geological Society, London, Special Publications*, 426:409–423, 2016.

[10] F. Bouchut and S. Boyaval. A new model for shallow viscoelastic fluids. *Mathematical Models and Methods in Applied Sciences*, 23:1479–1526, 2013.

[11] M. Boutounet, J. Monnier, and J.-P. Vila. Multi-regime shallow free surface laminar flow models for quasi-Newtonian fluids. *European Journal of Mechanics-B/Fluids*, 55:182–206, 2016.

[12] G. Chambon. *Quelques contributions à la modélisation des écoulements à surface libre de fluides complexes*. PhD thesis, HDR en Sciences de la Planète et de l'Environnement, Université de Grenoble I, 2014.

[13] G. Chambon, P. Freydier, M. Naaim, and J.-P. Vila. Asymptotic expansion of the velocity field within the front of viscoplastic surges: comparison with experiments. *Journal of Fluid Mechanics*, 884, 2020.

[14] H.-C. Chang and E. A. Demekhin. Complex wave dynamics on thin films. 2002.

[15] S. Cochard. Measurements of time-dependent free-surface viscoplastic flows down steep slopes. Technical report, EPFL, 2007.

[16] S. Cochard and C. Ancey. Experimental investigation of the spreading of viscoplastic fluids on inclined planes. *Journal of Non-Newtonian Fluid Mechanics*, 158:73–84, 2009.

[17] F. Couderc, J. Monnier, J.-P. Vila, K. Larnier, R. Madec, and D. Dartus. Robust Finite Volume schemes for 2D Shallow Water models. application to flood plain dynamics. *HAL-01133594*, 2015.

[18] B. De St Venant. Theorie du mouvement non-permanent des eaux avec application aux crues des rivers et a l'introduntion des marees dans leur lit. *Academic de Sci. Comptes Redus*, 73:148–154, 1871.

[19] E. D. Fernández-Nieto, P. Noble, and J.-P. Vila. Shallow Water equations for non-Newtonian fluids. *Journal of Non-Newtonian Fluid Mechanics*, 165:712–732, 2010.

[20] R. W. Griffiths. The dynamics of lava flows. *Annual Review of Fluid Mechanics*, 32:477–518, 2000.

[21] A. J. Harris and J. S. Allen III. One-, two-and three-phase viscosity treatments for basaltic lava flows. *Journal of Geophysical Research: Solid Earth*, 113, 2008.

[22] Q. Liang and F. Marche. Numerical resolution of well-balanced Shallow Water equations with complex source terms. *Advances in Water Resources*, 32:873–884, 2009.

[23] F. Marche. Derivation of a new two-dimensional viscous Shallow Water model with varying topography, bottom friction and capillary effects. *European Journal of Mechanics-B/Fluids*, 26:49–63, 2007.

[24] N. Martin and J. Monnier. Inverse rheometry and basal properties inference for pseudoplastic geophysical flows. *European Journal of Mechanics-B/Fluids*, 50:110–126, 2015.

[25] J. Monnier, F. Couderc, D. Dartus, K. Larnier, R. Madec, and J.-P. Vila. Inverse algorithms for 2D Shallow Water equations in presence of wet dry fronts: Application to flood plain dynamics. *Advances in Water Resources*, 97:11–24, 2016.

[26] J. Monnier, K. Larnier, L. Pujol, F. Couderc, and P.-A. e. a. Garambois. Dassflow, open-source computational software. *https://www.math.univ-toulouse.fr/DassFlow*.

[27] S. Morris, M. Sellier, and A. R. A. Behadili. Comparison of lubrication approximation and Navier-Stokes solutions for dam-break flows in thin films. *arXiv preprint arXiv:1708.00976*, 2017.

[28] P. Noble and J.-P. Vila. Thin power-law film flow down an inclined plane: consistent Shallow Water models and stability under large-scale perturbations. *Journal of Fluid Mechanics*, 735:29–60, 2013.

[29] H. Ozmen-Cagatay and S. Kocaman. Dam-break flow in the presence of obstacle: experiment and CFD simulation. *Engineering Applications of Computational Fluid Mechanics*, 5:541–552, 2011.

[30] J.-M. Piau. Flow of a yield stress fluid in a long domain. application to flow on an inclined plane. *Journal of Rheology*, 40:711–723, 1996.

[31] R. W. Pryor. *Multiphysics modeling using COMSOL®: a first principles approach*. Jones & Bartlett Publishers, 2009.

[32] L. Pujol, P.-A. Garambois, and J. Monnier. Multi-dimensional hydrological-hydraulic model with variational data assimilation for river networks and floodplains. *Geoscientific Model Development*, 15:6085–6113, 2022.

[33] G. Richard, C. Ruyer-Quil, and J.-P. Vila. A three-equation model for thin films down an inclined plane. *Journal of Fluid Mechanics*, 804:162–200, 2016.

[34] A. Rohatgi. Webplotdigitizer user manual version 3.4. *http://arohatgi. info/WebPlotDigitizer/app*, pages 1–18, 2014.

[35] E. F. Toro. *Riemann solvers and numerical methods for fluid dynamics: a practical introduction*. Springer Science & Business Media, 2013.

[36] C. B. Vreugdenhil. *Numerical methods for Shallow Water flow*, volume 13. Springer Science & Business Media, 1994.

A Appendix: the Finite Volume scheme

In this section, solution procedure for the Shallow Water equations using finite volume method of Godunov type is presented, following [17, 25, 35], see also [32].

A.1 Numerical scheme basic form

Firstly, the model is written in conservative form as

$$\partial_t \boldsymbol{U} + \partial_x \boldsymbol{F}(\boldsymbol{U}) + \partial_y \boldsymbol{G}(\boldsymbol{U}) = \boldsymbol{S}_g(\boldsymbol{U}) + \boldsymbol{S}_f(\boldsymbol{U}) \tag{A.1}$$

where
$\boldsymbol{U} = \begin{bmatrix} h \\ h\bar{u} \\ h\bar{v} \end{bmatrix}$ is the vector of conserved variables,
$\boldsymbol{F}(\boldsymbol{U}) = \begin{bmatrix} h\bar{u} \\ h\bar{u}^2 + \frac{1}{2}gh^2\cos\theta + C_m \left[\frac{\rho g}{K} S_{\theta_x}\right]^{2m} h^{2m+3} \\ h\bar{u}\bar{v} + C_m \left[\frac{\rho g}{K} S_{\theta_x}\right]^{2m} h^{2m+3} \end{bmatrix}$ and $G(\boldsymbol{U}) = \begin{bmatrix} h\bar{v} \\ h\bar{u}\bar{v} + C_m \left[\frac{\rho g}{K} S_{\theta_y}\right]^{2m} h^{2m+3} \\ h\bar{v}^2 + \frac{1}{2}gh^2\cos\theta + C_m \left[\frac{\rho g}{K} S_{\theta_y}\right]^{2m} h^{2m+3} \end{bmatrix}$
are the vectors of fluxes,
$\boldsymbol{S_g}(\boldsymbol{U}) = \begin{bmatrix} 0 \\ -gh\left(\cos\theta \frac{\partial b}{\partial x} - \sin\theta\right) \\ -gh\left(\cos\theta \frac{\partial b}{\partial y} - \sin\theta\right) \end{bmatrix}$ and $\boldsymbol{S_f}(\boldsymbol{U}) = \begin{bmatrix} 0 \\ -\frac{1}{\rho}\tau_{b_x} \\ -\frac{1}{\rho}\tau_{b_y} \end{bmatrix}$ are the vectors of sources. Basal shear stress$\boldsymbol{\tau}_b$ is given by (5.28).

Secondly, Godunov-type finite volume method is employed to solve the integrated form of the Shallow Water equations (A.1) which generally yields a semi-discretized equation of the form

$$\partial_t \mathbf{U} + \frac{1}{m_k} \sum_{e \in \partial k} m_e \hat{\boldsymbol{F}}_e(\boldsymbol{U}) = \boldsymbol{S}_g(\boldsymbol{U}) + \boldsymbol{S}_f(\boldsymbol{U}) \tag{A.2}$$

where, following notations defined in DassFlow [26]; Ω is the computational domain in 2D with N number of cells, k representing the cell index, m_k the area of the cell k, $m_{\partial k}$ perimeter of the cell k, k_e neighboring cell, e the cell edge, $\boldsymbol{n}_e$ the unit normal vector to e, $n_{e,k}$ the unit normal vector to e pointing outward from k to k_e, m_e the length of the side e, and $\hat{\boldsymbol{F}}_e(\boldsymbol{U}) = \boldsymbol{F}_e(\boldsymbol{U})\, n_{e_x} + \boldsymbol{G}_e(\boldsymbol{U})\, n_{e_y}$ the intercell normal flux obtained by applying the rotational invariance property in Eq. (A.1), see [35]. This property enables us to reduce the sum of a 2D problem to a 1D Riemann problem.

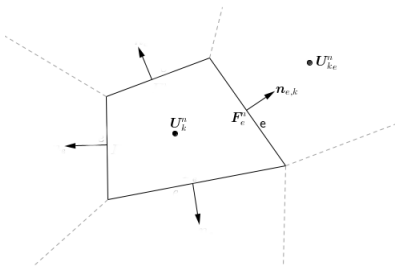

Figure 16: Finite volume cell k: showing notations used for mesh discretization

A.2 Splitting method

To obtain a fully discretized system of Eq. (A.2), splitting method is employed for numerical treatment of

the fluxes and the source terms. Splitting methods are commonly used to divide a long equation incorporating several time-dependent physical process into simpler equations for individual physical process, which can be solved separately by numerical techniques [22, 35]. Incorporating prediction and correction method, the splitting method here consists of two steps:
Step 1: Compute $\widetilde{\boldsymbol{U}}^{n+1}$ solution of (A.2) without the friction term:

$$\partial_t \mathbf{U} + \frac{1}{m_k} \sum_{e \in \partial k} m_e \hat{\boldsymbol{F}}_e \left(\boldsymbol{U} \right) = \boldsymbol{S}_g \left(\boldsymbol{U} \right) \tag{A.3}$$

Step 2: Given the predicted solution $\widetilde{\boldsymbol{U}}^{n+1}$, compute $\boldsymbol{U}_k^{n+1}$solution of

$$\partial_t \mathbf{U} = \boldsymbol{S}_f \left(\boldsymbol{U} \right) \tag{A.4}$$

It's noted that the solution$\widetilde{\boldsymbol{U}}^{n+1}$ obtained in Step 1 is used to update the solution $\boldsymbol{U}_k^{n+1}$ obtained in Step 2. This procedure is described in the next subsection and detailed in [26]. Following these steps, the expected final scheme in general will take the form

$$\boldsymbol{U}_k^{n+1} = \widetilde{\boldsymbol{U}}_k^{n+1} + \Delta t \boldsymbol{S}_f \left(\widetilde{\boldsymbol{U}}_k^{n+1} \right) \tag{A.5}$$

It is evident from Eq. (A.1) and (A.5) that for small fluid depth i.e as $h \to 0$, the friction term becomes very large compared to other terms and can lead to numerical instability. In that sense, a small time step Δt can be chosen to maintain stability, however this can be computationally expensive. To overcome this drawback, a proper numerical treatment of the friction source term is required i.e. the friction source term can be treated implicitly while others are treated explicitly.

A.3 Interface fluxes and gravity source term discretization

Here, the fluxes and gravity source terms are treated explicitly, thus, integrating Eq. (A.3) in time, a fully discrete system is obtained:

$$\widetilde{\boldsymbol{U}}^{n+1} = \boldsymbol{U}_k^n - \frac{\Delta t}{m_k} \sum_{e \in \partial k} m_e \hat{\boldsymbol{F}}_e \left(\boldsymbol{U}^n \right) + \Delta t \boldsymbol{S}_g \left(\boldsymbol{U}^n \right) \tag{A.6}$$

where subscript k represent the mesh cell index, superscript n is the time level, $\Delta t = t^{n+1} - t^n$ is the time step for $t \in [0, T]$, $\boldsymbol{U}_k^n$ the approximation of $\boldsymbol{U}$at time t^n, and $\hat{\boldsymbol{F}}_e = \hat{\boldsymbol{F}}_{e,k} - \hat{\boldsymbol{F}}_{e,k_e}$ are the numerical fluxes through the interfaces of cell k at time t^n. For clarity it is worth noting that this can also be written as$\hat{\boldsymbol{F}}_e \left(\boldsymbol{U}^n \right) = \hat{\boldsymbol{F}}_e \left(\boldsymbol{U}_{e,k}^n \right) - \hat{\boldsymbol{F}}_e \left(\boldsymbol{U}_{e,k_e}^n \right)$ where $\boldsymbol{U}_{e,k}^n$ and $\boldsymbol{U}_{e,k_e}^n$ are the vectors of the conservative variable on either side of edge e. Numerical scheme (A.6) is complete when numerical fluxes $\hat{\boldsymbol{F}}_e$ and gravity source term $\boldsymbol{S}_g$ are reconstructed using finite volume methods developed in the literature, see e.g. [26, 35]. For this work Godunov-type scheme incorporated with HLLC approximate Riemann solver is employed as detailed in DassFlow guide [26]. For the gravity source term, a well balanced scheme developed in DassFlow (and references there in) which is stable for simulations involving wet-dry fronts is also adopted. To ensure positivity of the fluid depth and preservation of the fluid at rest property, Audusse et al. [4] considered a hydrostatic balance between the momentum components of the fluxes and gravity source term: $\frac{1}{2} g \nabla h^2 = -gh \nabla b$, and proposed a well balanced gravity source term scheme of the form $\boldsymbol{S}_g \left(\boldsymbol{U^n} \right) = -gh \nabla b \simeq \frac{1}{m_k} \sum_{e \in \partial k} m_e \frac{g}{2} \left[\left(h_{e,k}^n \right)^2 - \left(h_k^n \right)^2 \right] \boldsymbol{n}_{e,k}$, where the well-balanced discretization of the bed slope if considering the

x-direction, can be viewed as $\frac{\partial b}{\partial x} \simeq \frac{b_{e,k}-b_k}{\Delta x} \simeq \frac{h_k-h_{e,k}}{\Delta x}$, with $h_{e,k}$ representing the reconstructed hydrostatic water depth, at the left hand side of the cell interface e. This is first-order gravity source term scheme implemented in Dassflow for Newtonian fluids.

In a similar approach, comparing with the Newtonian version in DassFlow ([26]) and Audusse et al. ([4]), a well-balanced discretization of the gravity source term $\boldsymbol{S}_g(\boldsymbol{U}) = -g(\cos\theta h\nabla b - h\sin\theta)$ for SWE model derived here is employed. For instance, considering the x- direction gravity term:

$$\begin{aligned}\boldsymbol{S}_g &= -g\left(h\cos\theta\frac{\partial b}{\partial x} - h\sin\theta\right),\\ &\simeq -g\left[\left(\frac{h_{e,k}+h_k}{2}\right)\left(\frac{h_k-h_{e,k}}{\Delta x}\right)\cos\theta - \frac{h_{e,k}+h_k}{2}\sin\theta\right],\\ &\simeq \frac{g}{2\Delta x}\left[\left(h_{e,k}^2-h_k^2\right)\cos\theta + \Delta x\left(h_{e,k}+h_k\right)\sin\theta\right].\end{aligned} \tag{A.7}$$

Thus, in general $\boldsymbol{S}_g(\boldsymbol{U^n}) = -gh^n(\cos\theta\nabla b - \sin\theta) \simeq \frac{1}{m_k}\sum_{e\in\partial k} m_e\frac{g}{2}\left[\left(\left(h_{e,k}^n\right)^2 - \left(h_k^n\right)^2\right)\cos\theta + m_e\left(h_{e,k}^n + h_k^n\right)\sin\theta\right]\boldsymbol{n}_{e,k}$. Substituting this into Eq. (A.6) yields

$$\widetilde{\boldsymbol{U}}^{n+1} = \boldsymbol{U}_k^n - \frac{\Delta t}{m_k}\sum_{e\in\partial k} m_e\hat{\boldsymbol{F}}_e(\boldsymbol{U}^n) + \frac{\Delta t}{m_k}\sum_{e\in\partial k} m_e\frac{g}{2}\left[\left(\left(h_{e,k}^n\right)^2 - \left(h_k^n\right)^2\right)\cos\theta + m_e\left(h_{e,k}^n + h_k^n\right)\sin\theta\right]\boldsymbol{n}_{e,k} \tag{A.8}$$

Using appropriate Riemann solver (HLLC), this scheme for the fluxes and gravity term together with other terms are implemented in Dassflow for Non-Newtonian version.
Note: For further details of the hydrostatic reconstruction and numerical methods used see [4, 26] and the references there in.

A.4 Friction source term discretization

A stable implicit-scheme for the friction source term is required to avoid numerical instability as $h \to 0$. Using appropriate numerical methods, Eq. (A.4) can be solved conveniently to get a numerical scheme for the friction term. In an expanded form, this equation writes

$$\begin{aligned}\frac{\partial h}{\partial t} &= 0,\\ \frac{\partial \bar{\boldsymbol{q}}}{\partial t} &= \boldsymbol{S_f}.\end{aligned} \tag{A.9}$$

where$\boldsymbol{S_f} = -\frac{1}{\rho}\boldsymbol{\tau}_b$. Its's noted that the component of the continuity equation is already zero i.e. $\frac{h^{n+1}-\widetilde{h}^{n+1}}{\Delta t^n} = 0$, which implies that we only need to seek a solution of the non-zero component of the momentum equation. The fluid depth is thus updated as

$$h^{n+1} = \widetilde{h}^{n+1}. \tag{A.10}$$

where $\widetilde{h}^{n+1}$ is the fluid depth estimated at previous time step in Step 1 above. Treating the friction source term implicitly i.e at time level t^{n+1} for all state variables, the semi-implicit time step scheme writes

$$\frac{h^{n+1}\bar{\boldsymbol{u}}^{n+1} - \widetilde{h}^{n+1}\widetilde{\boldsymbol{u}}^{n+1}}{\Delta t^n} = -\frac{1}{\rho}\boldsymbol{\tau}_b^{n+1},$$

where $\widetilde{h}^{n+1}$ and $\widetilde{\boldsymbol{u}}^{n+1}$ are the previous solutions at t^n obtained in **step 1** above. Further, this writes

$$\bar{\boldsymbol{u}}^{n+1} = \widetilde{\boldsymbol{u}}^{n+1} - \frac{\Delta t^n}{\widetilde{h}^{n+1}\rho}\boldsymbol{\tau}_b^{n+1}. \tag{A.11}$$

recalling that $\boldsymbol{\tau}_b$expression reads

$$\boldsymbol{\tau}_b^{n+1} = \frac{K}{D}\left(\frac{K}{\rho g\,|\,\boldsymbol{S}_\theta^n\,|}\right)^{m-1}\left(\frac{\tau_c}{\rho g||\,\boldsymbol{S}_\theta^n\,||} + h_c^n\right)\boldsymbol{q}^{n+1}. \tag{A.12}$$

Treating flow rate term implicitly, Eq. (A.11) becomes

$$\bar{\boldsymbol{u}}^{n+1} = \widetilde{\boldsymbol{u}}^{n+1} - \frac{\Delta t^n}{\rho\widetilde{h}^{n+1}}\left[\frac{K}{D}\left(\frac{K}{\rho g\,|\,\boldsymbol{S}_\theta^n\,|}\right)^{m-1}\left(\frac{\tau_c}{\rho g||\,\boldsymbol{S}_\theta^n\,||} + h_c^n\right)\widetilde{h}^{n+1}\bar{\boldsymbol{u}}^{n+1}\right]. \tag{A.13}$$

After rearrangement this results to

$$\bar{\boldsymbol{u}}^{n+1} = \widetilde{\boldsymbol{u}}^{n+1}\left(\frac{\rho D}{\rho D + \Delta t^n K\left(\frac{K}{\rho g\,|\,\boldsymbol{S}_\theta^n\,|}\right)^{m-1}\left[\frac{\tau_c}{\rho g\,||\,\boldsymbol{S}_\theta^n\,||} + \widetilde{h}_c^{n+1}\right]}\right). \tag{A.14}$$

As $h \to 0$ then $\bar{\boldsymbol{u}}^{n+1} \to 0$, which implies that the fluid at rest property is preserved even at wet/dry fronts. This develops to the following full-implicit scheme

$$\mathbf{U}_k^{n+1} = \begin{pmatrix} h^{n+1} \\ h^{n+1}\bar{\boldsymbol{u}}^{n+1} \end{pmatrix} = \begin{bmatrix} \widetilde{h}^{n+1} \\ h^{n+1}\widetilde{\boldsymbol{u}}^{n+1}\left(\frac{\rho D}{\rho D + \Delta t^n K\left(\frac{K}{\rho g\,|\,\boldsymbol{S}_\theta^n\,|}\right)^{m-1}\left[\frac{\tau_c}{\rho g\,||\,\boldsymbol{S}_\theta^n\,||} + \widetilde{h}_c^{n+1}\right]}\right) \end{bmatrix}. \tag{A.15}$$

Recall the critical depth h_c , S_θ term and the denominator D expressions are defined in Sec. 5. In a similar way, this scheme is also implemented in DassFlow together with other terms and results computed as presented in the previous section.

Remark: It is worth noting that only regime A is implemented in DassFlow. Further work need to be done to implement regime B in DassFlow.